Electrochemically Grown Tin Oxide Thin Films: In Situ Characterization of Electronic Properties and Growth Mechanism

Raül Díaz,[†] Suzanne Joiret,[‡] Ángel Cuesta,[§] Ismael Díez-Pérez,[†] Philippe Allongue,[‡,||] Claudio Gutiérrez,[§] Pau Gorostiza,[†] and Fausto Sanz*,[†]

LCTEM, Departament de Química Física, Universitat de Barcelona, Martí i Franquès 1, 08028-Barcelona, Spain, Laboratoire des Systèmes et Interfaces Electrochimiques, UPR 15 du CNRS, Université Paris 6, 4 Place Jussieu, Tour 22, 75005 Paris, France, and Instituto de Química Física "Rocasolano", CSIC, C. Serrano 119, 28006 Madrid, Spain

The oxidation and reduction processes of both polycrystalline tin and Sn(100) single crystals are investigated in borate buffer solution of pH 7.5 using cyclic voltammetry and in-situ characterizations such as Raman scattering, potential modulated reflectance spectroscopy (PMRS), and electrochemical scanning tunneling microscopy (EC−STM). Cross correlation of data yields new insights into the composition of the tin oxide film and its electronic properties as a function of oxidation conditions. We have unambiguously characterized the formation of at least three different tin oxides defined by the applied oxidation potential range with differentiated chemical composition and electronic properties. The first two oxidation peaks correspond to the formation of a tin hydroxide clearly detected by PMRS—that we propose to be a mixed Sn(II) oxy-hydroxide—leading, at intermediate oxidation potentials, to the formation of a fluorescent oxide that we propose to be a Sn(IV) oxide with deep states in the middle of the semiconductor band gap, the doping concentration depending on both the applied potential and the oxidation time. At far anodic potentials, a hydrated and nanocrystalline tin (IV) oxide is also unambiguously characterized.

1. Introduction

Research addressed to understand the electrochemical behavior (passivation, corrosion) of metallic tin is of considerable interest, since tin is a fairly corrosion-resistant metal, widely used in industrial applications. The corrosion resistance of tin in humid atmospheres and in aqueous solutions is attributed to the formation of a passive oxide/hydroxide film on the metal surface.[1] In conductive oxides, such as tin oxide, the understanding of electronic properties is an important issue, as it affects electrochemical transfer and corrosion in particular. Anodic films are most frequently nonstoichiometric, of amorphous or polycrystalline structure.[5] The principles of band theory of solids have been quite successfully extended to this type of materials[6] and the presence of a semiconducting oxide film determines the charge distribution and the potential drop across the metal-oxide−electrolyte interfaces. In SnO_2, conduction and surface properties have also an important impact in microelectronics and optical film semiconductor technology since this material has wide applications in optics,[2] solar cells,[3] and gas sensors.[4]

The electrochemical oxidation of tin has been studied in different electrolytic media.[7] The anodic passivation of tin in alkaline solutions is a complex, multistep process forming different oxide layers on the metal surface whose composition and thickness depend on applied potential and solution pH.

There is, however, still some controversy regarding the film composition and electrochemical oxidation pathways. The Pourbaix diagram of tin-water system[8] provides a starting point to understand passivation conditions. According to Pourbaix diagram, tin should passivate in neutral solution, since both tin oxides and hydroxides have an amphoteric nature, becoming dissolved as Sn^{2+} or Sn^{4+} at acidic pH values, and as stannites or stannates at alkaline pH values. The bibliography concerning the study of tin in slightly alkaline solutions, such as borate solutions, is extensive.[9−13] Early studies suggested that the initial stages leading to passivity could be ascribed to a dissolution−precipitation mechanism of either $Sn(OH)_2$ or SnO.[1,9,10] Models involving two parallel processes, metal dissolution and oxide formation, have been discussed.[11] Stirrup and Hampson[1] suggested that the first oxidation stage of tin is a dissolution−precipitation of SnO (or $Sn(OH)_2$) in strongly alkaline solutions, while the second stage is a solid-state process leading to the formation of a $Sn(OH)_4$ film. Permanent passivity results from a SnO_2 layer covering metallic tin. Stirrup and Hampson stated that the oxidation process leads to a mixed passive film formed by a continuous SnO_2 film sandwiched between the metal and a discontinuous SnO or $Sn(OH)_2$ film. However, XPS studies reported by Ansell et al.[12] suggested that the passive film only contains SnO_2 and $Sn(OH)_4$ species, with no Sn(II) species.

Nowadays, it seems accepted that the first two oxidation peaks at low anodic potentials result in a Sn(II) hydroxide after the first peak and in a thin layer of Sn(IV) hydroxide after the second peak. For example, in alkaline solutions, Shams El Din and Abd El Wahab[14] concluded that the primary passivation of tin occurs when the metal is covered with a $Sn(OH)_2$ or SnO film, and then permanent passivity is achieved with a continuous layer of $Sn(OH)_4$ covering the surface. Varsanyi et al.,[13a] using

* To whom correspondence should be addressed. Phone: ++34934021240; fax: ++34934021231; e-mail: fsanz@ub.edu.
† Universitat de Barcelona.
‡ Université Paris 6.
§ Instituto de Química Física "Rocasolano".
|| Permanent address: Laboratoire de Physique de la Matière Condensée (UMR 7643 CNRS), Ecole Polytechnique, F-91128 Palaiseau (France).

Mössbauer spectroscopy, speculated that films formed at low anodic potentials have a duplex structure, consisting both of amorphous $Sn(OH)_2$ or hydrated SnO layer and of SnO_2 or Sn-$(OH)_4$ film. At higher potentials, the passive layer consists only of Sn(IV) hydroxide or oxide. The most stable species under anodic polarization is $SnO_2 \cdot H_2O$[15] and, as dehydration of Sn-$(OH)_4$ to SnO_2 is highly irreversible, it can be assumed that the partial dehydration to $SnO_2 \cdot H_2O$ may be spontaneous. Electron diffraction studies of films formed during oxygen evolution[16] showed films to be duplex, consisting of a thick, poorly adherent and generally amorphous $5SnO \cdot 2H_2O$ film overlaying a thin and strongly adherent nanocrystalline $SnO_2 \cdot H_2O$ film.[16,17] More recently, it has been reported that tin behaves as a valve metal and that oxide growth involves field-assisted migration of ions through the oxide.[13f] Oxide films were nonstoichiometric with an excess of tin atoms or oxygen vacancies that results in n-type conductivity.[7d]

More recently,[18] we presented a new electroless deposition method to obtain nanocrystalline metal islands on SnO_2 nanopowders that can improve gas-sensing response. As electrochemistry enables characterization of the electronic properties for semiconductor oxides, we investigated tin oxide layers grown in borate buffer solution at pH 7.5 taking advantage of their stability in these media and our previous experience on the growth of both anodic iron[19] and tin[20] oxide films. For this study, we have chosen different characterization techniques that have been widely used for the elucidation of other electrochemical processes. We present here correlations between new experimental data that include cyclic voltammetry, in-situ Raman scattering, and in situ potential modulated reflectance spectroscopy (PMRS) studies, together with some in situ ECSTM results to investigate the growth mechanism and electronic properties of tin oxide layers formed at various anodic potentials.

Ex-situ Raman[21] and XPS[13] studies of tin anodic oxide and also a few in-situ studies, using Mössbauer,[9a] FTIR,[22] and Raman,[20a,21] have been reported. Ex-situ Raman spectroscopy has been widely employed to study oxidation states of tin in sensors and catalysts, mainly to distinguish between different tin oxides.[23] An extensive bibliography about in-situ Raman studies of passive films on nickel[24] or manganese[25] and semiconductors[26] is also available. On the other hand, PMRS has been applied, for example, to study CO adsorption on noble metal electrodes[27] and the electrochemical oxidation of Ti,[28] Fe,[29] or Ni.[30] In semiconductors, electroreflectance (ER) can be interpreted using Aspnes' model to determine band structure parameters.[31] In metals, PMRS is extremely surface-sensitive, because static electric fields are screened within the first atomic layer because of the high charge carrier density (the Thomas–Fermi screening length is ca. 0.05 nm for metals). Interpretation of PMR spectra in metals is much more difficult than in semiconductors. In the first place, with the exception of Cu, Ag, and Au, ER of metals is low and structureless and no model has been reported to interpret the spectra. However, important information about metal electrode interfaces with thin films can be gained by a simple visual inspection of the PMR spectra.[32]

2. Experimental Section

Ten millimeters diameter disks of both polycrystalline tin and Sn(100) samples (99.999%, Goodfellow) were employed for this study. Prior to electrochemical measurements, Poly-tin was mechanically polished using alumina powder down to a grain size of 0.3 μm. Surfaces were then chemically polished for 30 min in a solution previously described.[33] The resulting surfaces have areas of very low roughness (rms ~ 3 nm for areas of 25

μm^2). Sn(100) surfaces were prepared by slightly modifying previously reported methods.[34] All samples were then cleaned in hot trichloroethylene and acetone and two times in ethanol under agitation in an ultrasonic bath. A final water rinse was performed before drying under argon flow.

Electrochemical experiments were conducted under potentiostatic conditions in a boric/borate buffer solution at pH 7.5 and at room temperature. A standard three-electrode cell was used with a platinum grid as counter electrode and Ag/AgCl electrode (Metrohm) as reference of potentials. All potentials in the text are quoted versus this electrode. The cell was connected to a computer-controlled potentiostat (AUTOLAB PGSTAT12, Echochemie, The Netherlands). All results are expressed in terms of the projected geometrical area (1 cm²). Solutions were prepared using Milli-Q water and by mixing solutions of 0.35 M H_3BO_3 (p.a. grade, Merck) and 0.0375 M $Na_2B_4O_7 \cdot 10H_2O$ (p.a. grade, Merck). Prior to measurements, the solutions were bubbled with Argon to remove oxygen. All experiments were performed under static hydrodynamic conditions.

In-situ Raman spectroscopy was performed using a Jobin-Yvon Labram spectrometer with either a He–Ne (632.81 nm) or an argon (514.5 nm) laser. A 2-mm-thick electrolyte layer covered the sample and a diluted borate solution was used to reduce the contribution of borate anions. The laser light was focused on the surface and collected with a ULWD Olympus objective (×50). The incident laser power was set at 10 mW. The spot size with ×50 magnifications is 2-μm diameter in air and is increased in solution according to Fresnel laws.

In-situ PMR spectra were measured with unpolarized light in a two-window (Spectrosil B) cell at an angle of incidence of 45°. The light source was a 30 W deuterium lamp (Hamamatsu) mounted in a convective lamp housing (Oriel, model 60000) with a condensing lens/collimating lens accessory. A photomultiplier tube (Hamamatsu, model 1P28) was used. A sine wave (amplitude: 50 mV$_{rms}$; frequency: 65 Hz) was superimposed to the electrode potential. The modulated reflectance signal was detected with a digital lock-in amplifier (Stanford SR 850 DSP). Spectra are shown as the relative change in reflectance, ($\Delta R/R$), versus wavelength. (ΔR is the absolute change produced by the potential modulation in the reflectance, R, of the electrode).

In-situ EC–STM studies were performed at room temperature by using a Molecular Imaging microscope head (Phoenix, AZ) controlled by Nanoscope IIIa electronics (Digital Instruments Veeco Metrology Group, Santa Barbara, CA). The STM electrochemical cell was made of Teflon and exposed a sample area of 0.42 cm² to the solution through an O-ring. A Pt wire is used as a counter electrode, and a homemade true Ag/AgCl reference electrode with a double membrane to avoid chloride contamination was incorporated. STM tips were prepared by electrochemical etching of a Pt/Ir 80:20 wire following a method previously developed in our laboratory.[35] Tips prepared with this method present a large working potential range. The measured tip current at potentiostatic conditions was much lower than 0.1 nA. All STM images were recorded in the constant current mode at typical tunneling set-point currents ranging from 1 to 3 nA.

3. Results

3.1. Electrochemical Characterization. Figure 1 shows the cyclic voltammetric (CV) response of a polycrystalline tin in a borate buffer solution at pH 7.5. To compare unambiguously the voltammograms, prior to each CV, samples were prepolar-
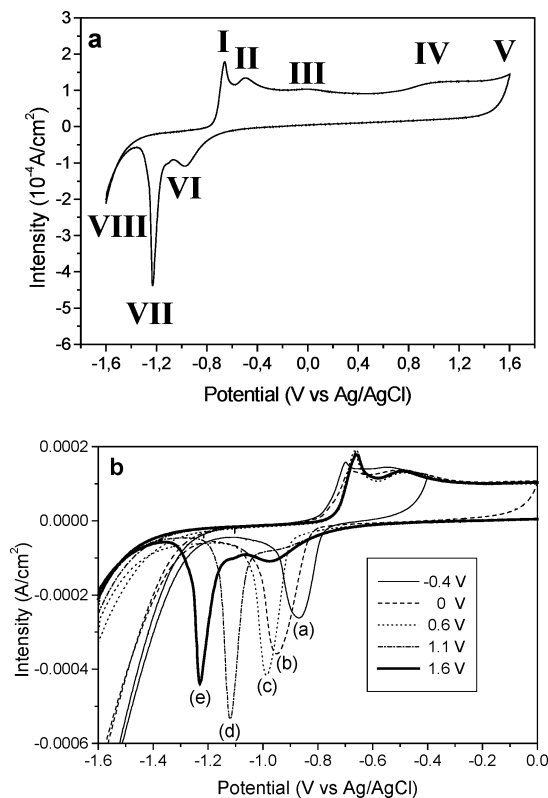
Figure 1. Cyclic voltammograms of metallic tin in borate buffer solutions at pH = 7.5. Potential scan rate 15 mV/s: (a) labeling; (b) influence of the potential positive limit U_A. For the sake of clarity, only some of all the investigated voltammograms are shown, i.e., those corresponding to $U_A = -0.4$ V (curve a), 0 V (curve b), 0.6 V (curve c), 1.1 V (curve d), and 1.6 V (curve e). See text for explanation concerning experimental procedure.

ized at -1.6 V for 15 min, then the applied potential was scanned from -1.6 V to the anodic potential limit (U_A) and back again to -1.6 V. Figure 1 then shows a scan being almost identical to all subsequent scans while the first cycle would be influenced by the pretreatment. Four anodic peaks (labeled as I−IV) and two cathodic peaks (labeled as VI and VII) are resolved (Figure 1a). Oxygen and hydrogen evolutions are labeled as regions V and VIII, respectively. The set of peaks is qualitatively similar to that previously reported in the same medium.[13] Curves a−e in Figure 1b are obtained changing the anodic potential limit U_A to more positive potentials. We observe that peak VII and hydrogen evolution reaction (HER) region VIII are strongly dependent on the U_A value. Indeed, both processes are shifted to more negative potentials as U_A is increased. Peak VI is a broad and low current peak masked by peak VII and it appears as a shoulder and emerges as a peak when the anodic potential limit is increased to $U_A \sim 1$ V. In the following, $U(i)$ defines the potential of peaks with $i =$ I−VIII.

To investigate the reduction peaks, the sample potential was stepped from -1.6 V to the anodic limit U_A before scanning back the potential to -1.6 V at various scan rates. Polarization time at U_A was 10 min for a scan rate of 5 mV/s, and either 10 min, 1 min, or 10 s for a scan rate of 15 mV/s. The cathodic scans are similar to those in Figure 1a. Figure 2 shows how some electrochemical variables vary with the anodic potential limit U_A. Figure 2a plots $U(VII)$ (open symbols) and the current density j (at $U = -1.59$ V) (filled symbols) as a function of U_A. Although the current density in the HER region increases exponentially with the potential, the plots of both $U(VII)$ and j (at $U = -1.59$ V) are remarkably invariant to the different scan
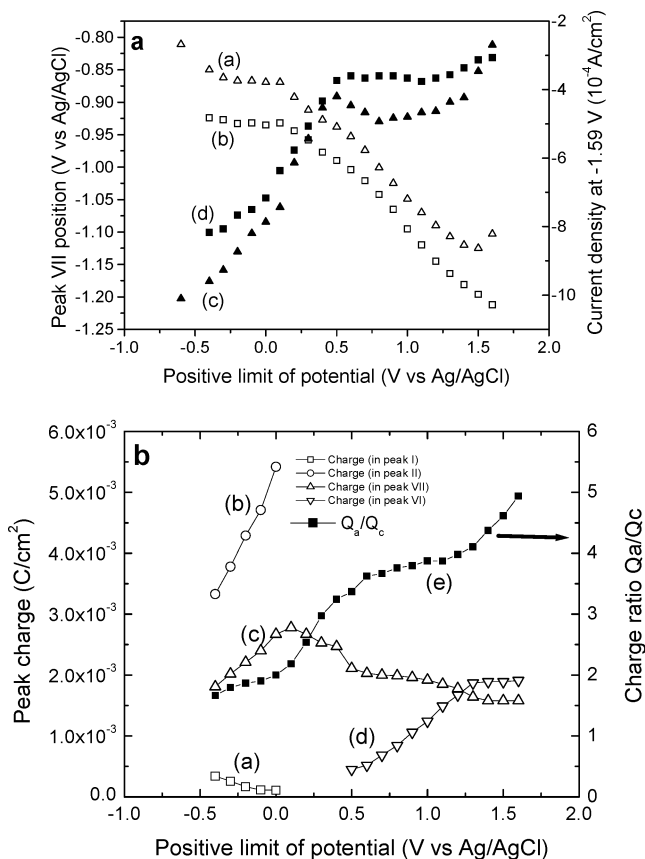

Figure 2. (a) Peak VII potential (open symbols) and HER cathodic current density measured at -1.59 V (filled symbols) as a function of U_A. In both cases, square symbols represent data acquired at 15 mV/s scan rate after oxidizing 10 s, while triangles represent data at 5 mV/s scan rate after oxidizing 10 min. (b) Plot of calculated charges on a voltammogram acquired at 15 mV/s, together with the ratio between the anodic/cathodic (Q_a/Q_c) charges. In all cases, curves are also labeled with letters to facilitate the discussion of the results.

rates and waiting times. Figure 2a shows two limiting cases, the lowest scan rate and longest oxidation time (5mV/s, 10 min) versus the fastest scan rate and shortest oxidation time (15 mV/s, 10 s). Clearly, two regions of anodic potential limit can be identified: for $U_A < 0.2$ V, $U(VII)$ is approximately constant and j (at $U = -1.59$ V) decreases (in absolute value) in an approximately linear behavior. For $U_A > 0.2$ V, $U(VII)$ shifts linearly toward negative potentials and j (at $U = -1.59$ V) stabilizes.

Figure 2b shows the variation against U_A of the integrated charge measured under peaks I, II, VI, and VII. The ratio Q_A/Q_C, with Q_A being the total anodic charge and Q_C the sum of the integrated charges for peaks VI and VII (which is practically close to the total cathodic charge), is also plotted in the same figure. The results have been measured for the highest scan rate because in this case irreversibility is enhanced.

3.2. In-Situ Raman Measurements. All in-situ Raman spectra were obtained without any SERS effect. Again, the samples were prepolarized at -1.6 V for 15 min; the sample potential was then ramped to U_A and maintained for 10 min before acquiring the spectral data. All Raman spectra exhibit a similar peak at 200 cm^{-1} corresponding to the cutoff from the notch filter and a small band at 880 cm^{-1} corresponding to polymeric borate anions.[36] The other features are electrode and eventually potential specific.

Figure 3a shows the influence of the applied potential in polycrystalline tin. For $U < U(III)$, the spectrum is featureless
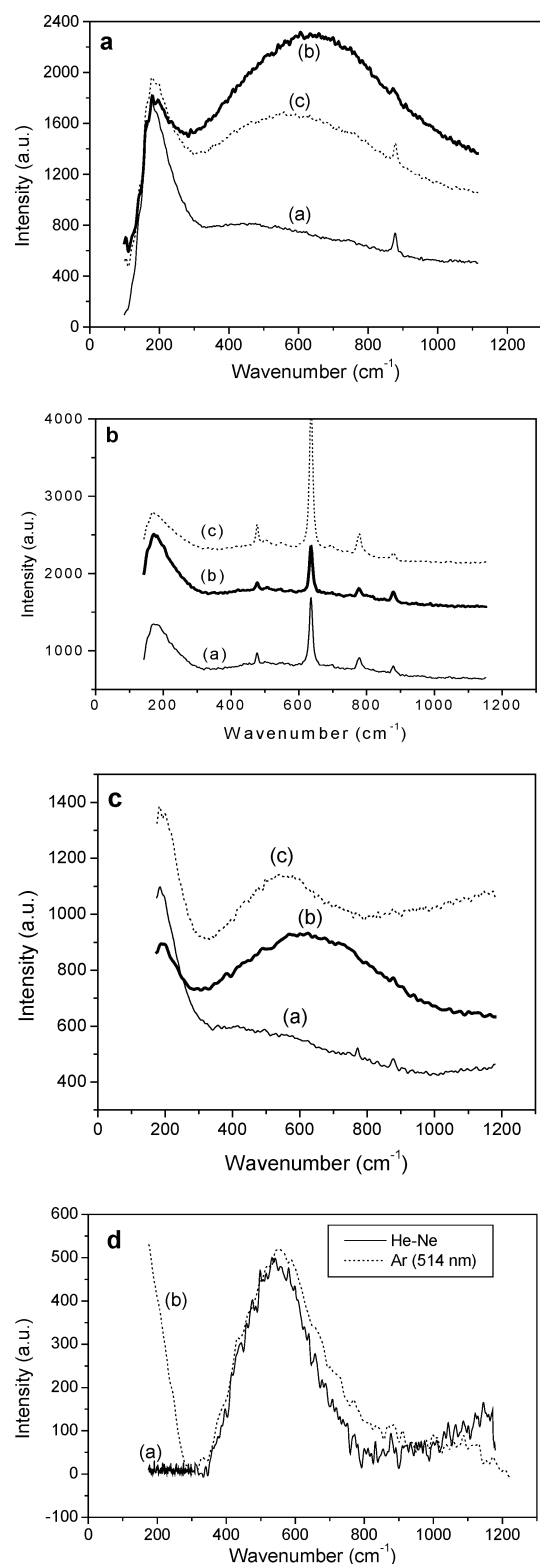
Figure 3. Results of the in-situ Raman characterization of the surfaces: (a) Tin polycrystal at different applied positive potential limits when using a He−Ne laser: −−, −1.1 V (curve a); −−, 0.3 V (curve b); •••••, after keeping the potential at 0.3 V during 30 min (curve c). (b) Thermally grown Sn oxide layer with a He−Ne laser: −−, OCP (−0.18 V) (curve a); −−, 0.3 V (curve b); •••••, 1.1 V (curve c). (c) Sn(100) with a He−Ne laser: −−, −1.1 V (curve a); −−, 0.3 V (curve b); •••••, 1.1 V (curve c). (d) Comparison of the Raman peaks detected after oxidizing Sn(100) at 1.1 V with a He−Ne (curve a) and an argon (514 nm) (curve b) laser. These last spectra are obtained after subtracting the background.

as the one measured at −1.1 V (curve a). For oxidation potentials $U(III) < U < U(IV)$, a new broad band (fwhm =

640 cm^{-1}) centered at 650 cm^{-1} appears (curve b). The intensity of this band diminishes upon prolonged oxidation at 0.3 V (curve c). It also disappears upon reducing the film at −1.6 V for 15 min and a spectrum similar to the one observed at −1.1 V is obtained. Reoxidation at 0.3 V restores the band, thus indicating that the process is nearly reversible provided the anodic potential excursion is short. Prolonged oxidation at 1.1 V (10 min) quenches the band irreversibly (spectrum similar to curve a). No anti-Stokes counterpart of this band has been observed. Figure 3b shows Raman spectra obtained with a thermal SnO$_2$ layer prepared by annealing polycrystalline tin in air at 800 °C for 10 min. Spectra are independent of applied potential (potentials more negative than the open circuit potential (OCP) were not investigated to avoid reduction of the oxide). They show the expected Raman bands for SnO$_2$: A$_{1g}$ (630 cm^{-1}), B$_{2g}$ (774 cm^{-1}), and E$_{1g}$ (472 cm^{-1}).[37]

The electrochemistry of Sn(100) single crystal has been investigated in parallel with polycrystalline tin in borate buffer solutions at pH 7.5 and the voltammetric response is qualitatively the same,[34] but in-situ Raman characterization of the anodic oxides gives a difference upon oxidation of Sn(100) at $U > 1$ V during 10 min. Figure 3c shows that Raman spectra obtained with Sn(100) at intermediate potentials behaves the same as potential dependence with a broad band at 650 cm^{-1}, but a new band is observed (Figure 3c, curve c) around 580 cm^{-1}, at more anodic potentials. This band does not disappear immediately at negative potentials, even when scanning down to −1.6 V. Figure 3d shows the influence of the excitation wavelength in a Sn(100) electrode. Changing to green laser lets appear again the broad band centered at 580 cm^{-1} if a potential $U = 1.1$ V is applied enough times. After background subtraction, there is almost no difference with respect to the spectrum obtained with red laser.

3.3. In-Situ Potential Modulated Reflectance. The experiments reported here were conducted using UV/vis radiation on polycrystalline tin electrodes using the same experimental routine of potential application as in the in-situ Raman experiments. Results focus on the UV region of spectra, where some influence of the potential was found. In the visible region (440 nm < λ < 800 nm), spectra were structureless (not shown). Figure 4 presents PMR spectra recorded on polycrystalline tin at various potentials. No signal is detected until $U_A = -0.5$ V (Figure 4a). At this potential, a maximum in $\Delta R/R$ appears around 300 nm (4.13 eV), whose position shifts linearly toward higher energies with increasing applied potential between −0.5 and 0 V (Figure 4b). The peak starts to disappear at $U_A = 0$ V and is absent as soon as $U_A > 0.2$ V (Figure 4c). For $0.2 < U_A < 0.7$ V, there is no clear feature in the PMR spectra, but a clear minimum appears around 340 nm at $U_A > 0.8$ V (Figure 4d).

3.4. In-Situ EC−STM. Figure 5 shows the STM images registered during a voltammetric cycle for the selected potentials indicated by arrows on the voltammogram. A Sn(100) single-crystal surface was used to distinguish the oxide overlayer. Image a of the initial tin surface shows the metallic tin terraces with a separation of 0.32 nm. The electrochemical procedure is similar to that described for the other in-situ techniques. An initial reduction pretreatment at −1.6 V for 15 min and then scanning at 5 mV/s up to −0.2 V and scan reversing are the steps for voltammogram acquisition. Images a and c were collected at constant potential and are the first images acquired for the corresponding electrode potential. Subsequent images are stationary. In images b and d, while scanning the image from top to bottom, the potential was scanned from −1 V
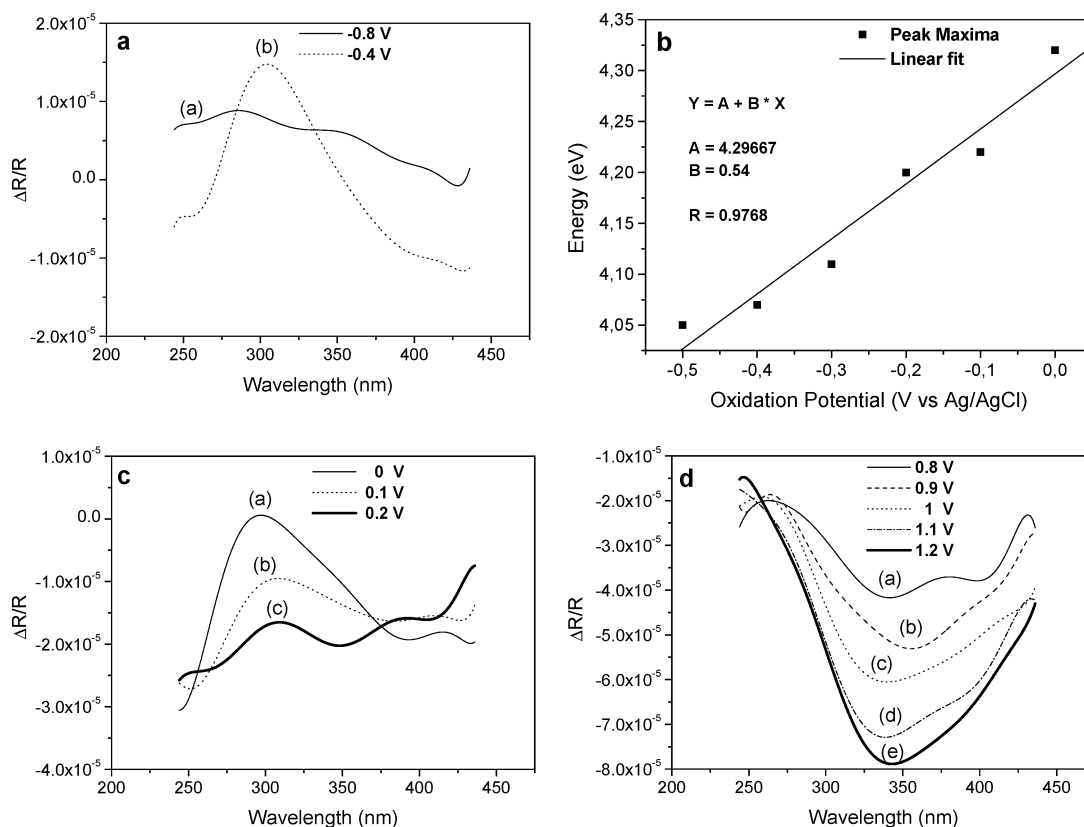
Figure 4. In-situ PMR spectra of polycrystalline tin. The spectra shown here have been smoothed fitting the experimental spectra to a polynomial of degree 9. (a) Spectra at −0.8 (curve a) and at −0.4 V (curve b); (b) plot of the energy of the maximum observed in the PMR spectra between −0.5 and 0 V vs the electrode potential; (c) spectra between 0 and 0.2 V (curves a−c); (d) spectra between 0.8 and 1.2 V (curves a−e).
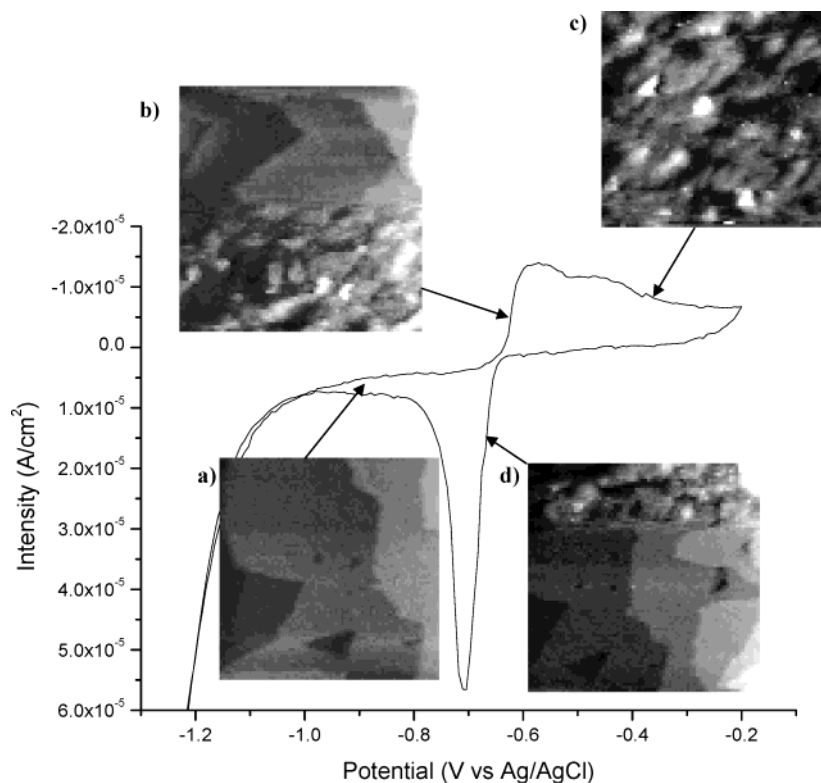

Figure 5. In-situ EC−STM images of the tin oxide layer. Potentials were reached by scanning at 5 mV/s: (a) image of the initial metallic surface at −1 V; (b) first image after scanning up to −0.6 V. Subsequent images are similar to image c; (c) image after scanning up to −0.3 V; (d) first image after reversing the scan to −0.8 V. Subsequent images are similar to image a. All the images have been acquired from top to bottom. XY range of 300 nm × 300 nm and Z gray scale represents 2 nm.

(stepped tin surface) to the arrow potential to make clear the formation b and from the reversing potential to the arrow

potential to make clear the deformation d of the oxide layer. Linear variation of potential while imaging was used in place

of a potential step just to overcome abrupt charging currents that eventually may affect tip bias potential.

4. Discussion

As mentioned in the Introduction, the formation of a $Sn(OH)_4$ film at potentials corresponding to our peak II was claimed in recent publications,[13] thereby attributing the oxidation peaks at more positive potentials to film dehydration and doping changes. Nevertheless, when correlating the in-situ results here reported, a different interpretation arises clearly showing the presence of at least three distinguishable oxide layers whose stability depends on the applied potential range (U_A). Thus, the discussion will be separated in three parts to show the correlation of the results for the three in-situ techniques within the corresponding range:

4.1. Oxidation at $U_A < U(III)$. The initial oxidation of metallic tin in borate buffer solutions takes place in two overlapped voltammetric peaks (I and II), assigned in the more recent publications[13] to reactions $Sn(0) \rightarrow Sn(II)$ (peak I) and $Sn(II) \rightarrow Sn(OH)_4$ (peak II), respectively. The unique reduction peak (peak VII) observed when the scan is reversed before reaching peak III has been attributed as corresponding to the reduction of both species to metallic tin.[13] No Raman signal is detected in this potential region, most probably because of the oxide morphology, as already imaged using in-situ EC−STM in Figure 5. The oxidation process taking place on the Sn(100) single-crystal gives an unordered oxide thin layer that, up to $U_A = -0.1$ V, is reduced again to the metallic well-defined tin surface by reversing the potential (see Figure 5d). The metallic character of the initial and final surfaces have been tested by in-situ EC−STS curves,[34] and the reversibility to the well-defined surface is lost when anodic potential limit $U_A > -0.1$ V. The oxide is formed by nanometer scale particles that covers the metallic surface with a film 1.5−2-nm thick by etching tin atoms from the steps. The film passivates the surface remaining almost invariant with time. No changing in the film thickness was detected when the potential was reversed at low scan rate and surface imaged as in Figure 5d. Conduction through the film is permanent for all the bias potentials allowed to the tip disregarding the presence of a band gap. The thin film structure can be responsible for the signal absence in Raman.

PMR spectra show a maximum to appear upon reaching the potential region corresponding to peaks I and II. The band maximum is around 300 nm and shifts toward higher energies as the potential is increased, with a slope of 0.5 eV·V^{-1}. This maximum disappears in the potential region corresponding to peak III (see figure 4a and 4b). In *oxide-free* metals, a peak in PMR spectra, the energy of whose maximum shifts linearly with the electrode potential, is usually interpreted as an electronic transition from an occupied bulk state to an empty surface state, if the energy of the transition increases with increasing electrode potential,[32] which is the case. Surface states can be intrinsic (when they arise as a consequence of lattice termination and appear in energy gaps) or extrinsic (when they arise from chemically different species at the surface). According to the simple model for oxide-free metals developed by Boeck and Kolb[39] that assumes a linear potential drop across the double layer with a double layer thickness of 3−5 Å, the positive linear dependence of the peak maximum around 300 nm shown in Figure 4b should correspond to an electronic transition from a filled bulk state to an empty surface state located halfway through the double layer, that is, 1.5−2.5 Å away from the metal surface. In the present case, in which the metal is covered by an oxide layer 10 times thicker, the location in the interface,

let alone the identification, of the surface states is far more questionable. In any case, the hypothesis of surface states would make sense if we had an adlayer of hydroxiles on the Sn surface, which may be a hydroxide-covered layer, or less probable a change in the profile of the potential drop at the interface. Anyway, the band itself is originated by the surface oxide.

As recently reported by some of us,[20b] the oxidation process involved in peaks I and II is connected with the formation of Sn(II) species, the differentiation in two peaks being more connected with the hydroxylation process. Image b in Figure 5 shows that the oxidation on the lower potentials of peak I produces the same morphological oxide but at lower speed as demonstrated by varying the image scan frequency from 2 to 10 Hz, the corresponding reduction peak being unique. In the same sense, PMR peak in Figure 4a is also unique. A stable Sn(II) oxide−hydroxide phase with molecular formula $Sn_6O_8H_4$ has been identified,[40] while Sn(IV) is only present as stannic acids, with molecular formula SnO_3H_2.[41]

The formed mixed Sn(II) oxy-hydroxide by a dissolution−precipitation mechanism (see images b and c in Figure 5) unordered cannot definitively be ascribed to the former because we are unable to obtain the PMR spectrum by diffuse reflectence.[29] Anyway, the PMR peak does not correspond with the position of the absorption edge (i.e., the band-gap) of SnO_2.[38]

4.2. Oxidation Potentials $U(III) < U_A < U(IV)$. When $U_A \geq 0.2$ V (i.e., in the plateau overcoming peak III), several effects are simultaneously observed. The HER current in a subsequent negative scan abruptly decreases in absolute value (Figure 2a) and the anodic/cathodic charge ratio abruptly increases (Figure 2b). The charge ratio increase is connected to a decrease of peak VII current and to that the position of peak VII starts to shift negatively (Figure 2a), so the reduction of tin oxide occurs then at more negative potentials. As expected from the slow kinetics of the oxide grown process, this behavior changes when scanning at lower rates. Thus, at 0.1 mV/s, the decrease of HER current almost disappears, the shift of peak VII still existing although it is less pronounced.[42] This indicates that the change in HER current is mainly due to the noncomplete reduction of the grown oxide before reaching HER potential range. The oxide covering metallic tin inhibits HER evolution on it.

The electronic contribution can be inferred from the broad band (fwhm = 640 cm^{-1}) centered at 650 cm^{-1} that has been detected by in in-situ Raman spectra on polycrystalline Sn electrodes and that we have attributed to radiative recombination processes.[20a] Thus, the anodic oxide formed in this potential range is capable of absorbing 1.95 eV (red) light, producing a broad band, about 600 cm^{-1} wide, of a light emission centered at 1.87 eV (see Figure 3a). Results with Sn(100) give a similar behavior as polycrystals under red light. This allows discarding the presence of SnO, since its band gap is 0.62 eV,[43] and therefore, although radiative recombination with red light is possible, it can only emit light at energies lower than 0.62 eV. A tentative explanation is the formation of tin(IV) oxide (n-type semiconducting oxide with a direct band gap of 3.6 eV[44]) with some electronic states located in the midgap region. Under this assumption, the fluorescence "Raman" band observed at 650 cm^{-1} with red laser could be attributed to radiative recombination between the conduction band and the midgap level or between the midgap level and the valence band. The first process is, however, more likely because of the n-type semiconducting behavior of tin(IV) oxide. The total quenching of the fluorescence band after a long anodic excursion at a high potential suggests that the deep trap is located in the bulk of the oxide (probably as stoichiometric defects) rather than being
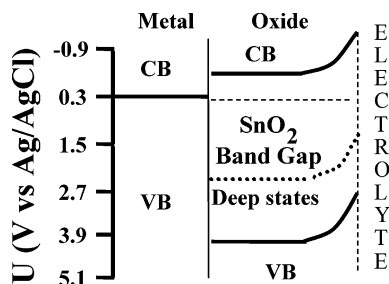
Electrochemically Grown Tin Oxide Thin Films

J. Phys. Chem. B, Vol. 108, No. 24, 2004 **8179**

Figure 6. Scheme of the quantitative band model for the Sn^0||tin passive film||electrolyte interface at an anodic potential limit $U_A = +300$ mV.

a surface state. Moreover, the fact that the Raman spectra of the thermal oxide under the same electrochemical conditions show the typical Raman spectrum of SnO_2[23] independently of the applied potential (Figure 3b) discards the attribution of the band detected in anodic oxides to a possible transition taking place in tin(IV) oxide where band bending diminishes the effective band gap.

The energy barrier created by the semiconducting layer at the electrode surface[45] can explain the electronic contribution to the shift of peak VII. In the negative sweep of the voltammogram, free electrons in the CB must overcome this barrier to reduce the oxide. Likely, as the positive potential limit U_A is increased between peak III and peak IV, the barrier could increase in thickness or height: the thickness of the space charge must be at least a few nm for the tunneling rate to be negligible. On the other hand, the increase in barrier height could be due to a shift of the CB edge away from the Fermi level, as a result of the progressive oxidation from Sn(II) to Sn(IV) (lower concentration of "oxygen vacancies" or Sn(II) sites, which act as donor dopant atoms, like Fe(II) in Fe(III) oxides[46]). Thus, it appears that in this case, Sn(II) progressively oxidizes to form a hydrated tin(IV) oxide SnO_x (where $1 < x < 2$). This behavior

is in agreement with the value of the CB edge potential, which is around -0.8V when oxidizing at $U_A = 0.3$ V (Figure 6), as directly measured by electron injection into the CB using EC−STS.[34] This value is not far from the flatband (FB) potential value of CVD-deposited SnO_2 calculated (indirectly) from photocurrent measurements[7d] (-1.4 V vs MSE at pH = 14, i.e., around -0.9 V vs Ag/AgCl at pH = 7.5) but differs considerably from the apparent FB potential of the electrochemical oxides measured using the same technique.[7d] This discrepancy could be due to electron traps in the band gap causing a shifting of the band edges beyond peak II, as schematized in the energetic band diagram shown in Figure 6. Further experiments using impedance spectroscopy and in-situ probe microscopy are being designed to test these points.[34]

Regarding in-situ PMR results, between 0.2 and 0.8 V the PMR spectra are structureless. Since at $U_A > 0.8$ V a different PMR spectra is present (Figure 4d), the results again support the presence at potentials between 0.2 and 0.8 V of an oxide different from the other two.

4.3. Potential Limit (U_A) More Positive than Peak IV. Oxidation beyond peak IV (around +0.9 V) causes to vanish the broad Raman bands detected at 0.3 V with both polycrystalline tin and Sn(100) single-crystal, appearing only in the Sn-(100) surface a new Raman band centered at 580 cm^{-1} (Figure 3c, curve c), suggesting that the structure of the film has influence on the results. Thus, Raman results can be explained by the formation of a new oxide layer that either (1) has a band gap higher than 2.4 eV and therefore cannot be excited (i.e., it is *transparent* to red or green laser) or (2) it does not have states allowing radiative recombination. As SnO_2 has a direct band gap of 3.6 eV, the formed oxide would be a hydrated tin(IV) oxide. This is confirmed by the fact that, when oxidizing the Sn(100) single crystal at these potentials, an identical Raman peak centered at 580 cm^{-1} is observed under red or green light,
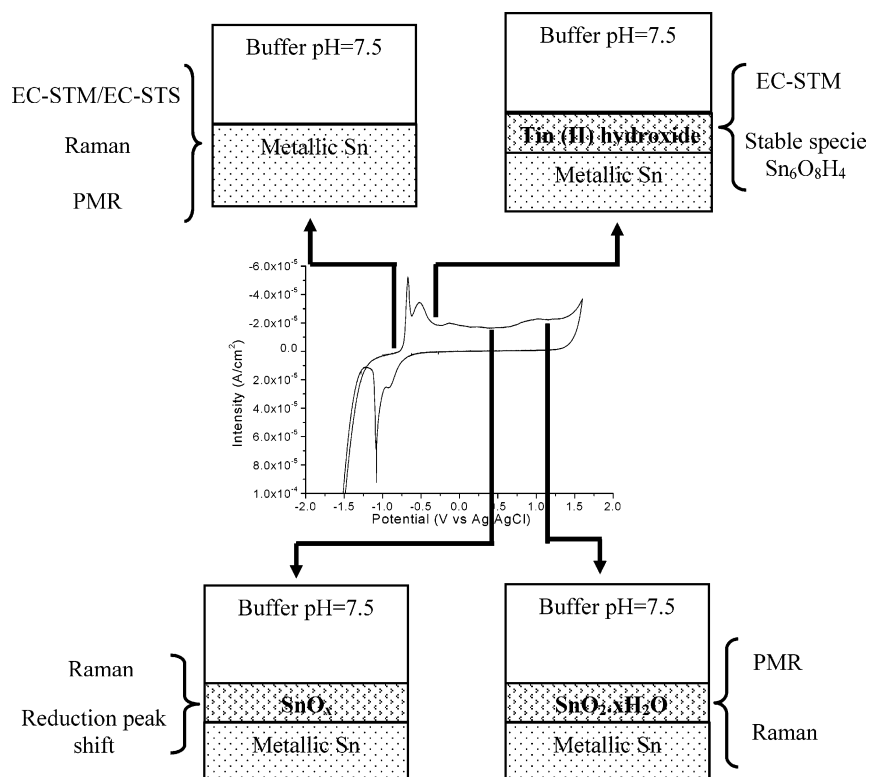

Figure 7. Scheme of the main phase present on the different anodic films, together with the characterization techniques that directly or indirectly supports the assignation.

which coincides with the position of the Raman peak of hydrated SnO$_2$ in nanocrystalline form.[21,47]

The formation of hydrated SnO$_2$ in peak IV is also supported by the PMRS results, since only when we reach these rather positive potentials a clear minimum appears around 340 nm (Figure 4d). This energy agrees well with that corresponding to the absorption edge (band gap) of a SnO$_2$ rutile structure ($\approx$335 nm if the light is polarized parallel to the *c* axis of the structure and $\approx$359 nm if it is polarized perpendicular to the *c* axis),[48] the intensity of the signal increasing with increasing potential, as expected if there would be a progressive increase of the oxide layer thickness. In any case, this Sn(IV) oxide is electrochemically stable, as indicated by the quenching of the fluorescence peak detected by Raman, the impossibility to recover it by electroreduction.

The hydrated Sn(IV) oxide promotes the stabilization of the HER current (Figure 2a) almost 4 times lower than the current observed on the metallic tin surface. While the appearance of peak VI in the negative scan can be ascribed to the reduction of Sn(IV) to Sn(II), the process is not complete and always a certain amount of Sn(IV) oxide remains causing the inhibition of HER. Finally, oxygen evolution current density measured at region V decreases while performing a second voltammetric cycle, thus confirming that oxide formed in peak IV is stable, the unreduced oxide accumulating on the surface from cycle to cycle. The changes in the potential shift of peak VII in HER current and in the anodic/cathodic charge ratio with respect to the potential limit, U_A, are due to a kinetic effect associated with the increase in thickness of the passive layer. In this range of potentials, the thickness of the formed oxide layers can increase significantly, that is, the curves I−t do not decrease to negligible values within some tens of seconds, as has been observed for the oxides formed at lower potential ranges.

5. Conclusions

The electrochemical oxidation and reduction processes of tin in borate buffer solutions at pH 7.5 have been systematically investigated using voltammetry, in-situ Raman scattering, in-situ potential modulated reflectance spectroscopy (PMRS), and in-situ EC−STM. The results allowed us to discuss the different oxides formed on the tin electrode surface and, for the sake of clarity, the final conclusion is shown in the scheme of Figure 7, where the behaving oxidation processes are assigned to a potential range. Our study has detected the formation of at least three different tin oxides depending on the applied oxidation potential range. We confirm that the first two oxidation peaks correspond to the formation of a mixed tin oxo-hydroxide not incorporating Sn(IV) and having fully reversibility. The non-linear shift of the largest reduction peak (peak VII) when increasing the anodic potential limit (U_A) of the voltammogram only happens at intermediate oxidation potentials. We attribute this shift to the formation of Sn(IV) oxides of decreasing doping concentration as both the applied potential and oxidation time increase. We propose a quantitative band diagram for the oxide interlayer that includes the presence of deep states in the mid of the band gap which cause the observed fluorescence when exciting with red laser light. Moreover, a hydrated and nano crystalline tin(IV) oxide is unambiguously characterized at the far positive potentials of peak IV. Systematic impedance and in-situ probe studies for understanding and quantifying the electronic properties of the passive film are currently under development.

References and Notes

(1) Stirrup, B. N.; Hampson, N. A. *J. Electroanal. Chem.* **1976**, *67*, 45.

(2) Sanon, G.; Rup, R.; Mansingh, A. *Phys. Status Solidi A* **1993**, *135*, 581.

(3) Jana, A. K. *J. Photochem. Photobiol., A* **2000**, *132*, 1.

(4) Göpel, W. *Sens. Actuators* **1989**, *16*, 167.

(5) Young, L. In *Anodic Oxide Films*; Academic Press: New York, 1961.

(6) Vijh, A. K. *Anodic Oxide Films: Influence of Solid State Properties on Electrochemical Behavior of Oxides and Oxide Films*; Diggle, J. W., Ed.; Marcel Dekker: New York, 1973; Vol. 2.

(7) (a) Seruga, M.; Metikos-Hukovic, M. *J. Electroanal. Chem.* **1992**, *334*, 223. (b) Metikos-Hukovic, M.; Omanovic, S.; Jukic, A. *Electrochim. Acta* **1999**, *45*, 977. (c) Seruga, M.; Metikos-Hukovic, M.; Valla, T.; Milun, M.; Hoffschultz, H.; Wandelt, K. *J. Electroanal. Chem.* **1996**, *407*, 83. (d) Burleigh, T. D.; Gerischer, H. *J. Electrochem. Soc.* **1988**, *135(12)*, 2938. (e) Giannetti, B. F.; Sumodjo, P. T. A.; Rabockai, T.; Souza, A. M.; Barboza, J. *Electrochim. Acta* **1992**, *37*, 143. (f) Bojinov, M.; Salmi, K.; Sundholm, G. *J. Electroanal. Chem.* **1993**, *358*, 177. (g) Giannetti, B. F.; Sumodjo, P. T. A.; Rabockai, T. *J. Appl. Electrochem.* **1990**, *20*, 672. (h) Drogowska, M.; Ménard, H.; Brossard, L. *J. Appl. Electrochem.* **1991**, *21*, 84.

(8) Pourbaix, M. In *Atlas of Electrochemical Equilibria in Aqueous Solutions*; Pergamon Press: Oxford, U.K., 1966.

(9) Goldschmidt, H.; Eckardt, G. *Z. Phys. Chem.* **1906**, *56*, 385.

(10) Foerster, F.; Dolch, M. *Z. Elektrochem.* **1909**, *16*, 599.

(11) Shah, S. N.; Davies, D. E. *Electrochim. Acta* **1963**, *8*, 703.

(12) Ansell, R. O.; Dickinson, T.; Povey, A. F.; Sherwood, P. M. A. *J. Electrochem. Soc.* **1977**, *124*, 1360.

(13) (a) Varsanyi, M. L.; Jaen, J.; Vertes, A.; Kiss, L. *Electrochim. Acta* **1985**, *30*, 529. (b) Kapusta, S.; Hackerman, N. *Electrochim. Acta* **1980**, *25*, 949. (c) Kapusta, S.; Hackerman, N. *Electrochim. Acta* **1980**, *25*, 1001. (d) Kapusta, S.; Hackerman, N. *Electrochim. Acta* **1980**, *25*, 1625. (e) Kapusta, S.; Hackerman, N. *J. Electrochem. Soc.* **1981**, *128(2)*, 327. (f) Kapusta, S.; Hackerman, N. *J. Electrochem. Soc.* **1982**, *129(9)*, 1886. (g) Metikos-Hukovic, M.; Resetic, A.; Gvozdic, V. *Electrochim. Acta* **1995**, *40*, 1777.

(14) Shams El Dim, A. M.; Abd El Wahab, F. M. *Electrochim. Acta* **1964**, *9*, 883.

(15) Sillen, L. G. *J. Chem. Educ.* **1952**, *29*, 600.

(16) Hampson, N. A.; Spencer, N. E. *Br. Corros. J.* **1968**, *3*, 1.

(17) Pugh, R.; Gabe, D. R.; Warner, M. *Corr. Sci.* **1967**, *7*, 807.

(18) (a) Díaz, R.; Arbiol, J.; Cirera, A.; Sanz, F.; Peiró, F.; Cornet, A.; Morante, J. R. *Chem. Mater.* **2001**, *13*, 4362. (b) Díaz, R.; Arbiol, J.; Sanz, F.; Cornet, A.; Morante, J. R. *Chem. Mater.* **2002**, *14*, 3277.

(19) (a) Díez-Pérez, I.; Gorostiza, P.; Sanz, F.; Müller, C. J. *Electrochem Soc.* **2001**, *148(8)*, B307. (b) Díez-Pérez, I.; Gorostiza, P.; Sanz, F.; Müller, C. J. In *Proceedings of the Symposium "Scanning Probe Microscopy for Electrode Characterization and Nanometer Scale Modification"*; Hansen, D. C., Isaacs, H. S., Sieradzki, K., Eds.; The Electrochemical Society Inc.: Pennington, NJ, 2001; Vol. 2000−35, p 122. (c) Díez-Pérez, I.; Gorostiza, P.; Sanz, F. *J. Electrochem Soc.* **2003**, *150 (7)*, B348.

(20) (a) Díaz, R.; Díez-Pérez, I.; Gorostiza, P.; Sanz, F.; Joiret, S.; Allongue, P. In *Proceedings of the Symposium "Mechanisms in Electro-chemical Deposition and Corrosion"*; Barbour, J. C., Penner, R. M., Searson, P. C., Eds.; Materials Research Society: Pittsburgh, PA, 2003; Vol. 781E, p Z1.3. (b) Díaz, R.; Díez-Pérez, I.; Gorostiza, P.; Sanz, F.; Morante, J. R.; *J. Braz. Chem. Soc.* **2003**, *14 (4)*, 523.

(21) Huang, B. X.; Tornatore, P.; Li, Y.-S. *Electrochim. Acta* **2000**, *46*, 671.

(22) Moina, C. A.; Ybarra, G. O. *J. Electroanal. Chem.* **2001**, *504*, 175.

(23) (a) Abello, L.; Bochu, B. Gaskov, A.; Koudryavtseva, S.; Lucazeau, G.; Roumyantseva, M. *J. Solid State Chem.* **1998**, *135*, 78. (b) Sangaletti, L.; Depero, L. E.; Allieri, B.; Pioselli, F.; Comini, E.; Sberveglieri, G.; Zocchi, M. *J. Mater. Res.* **1998**, *13(9)*, 2457.

(24) (a) Kostecki, R.; McLarnon, F. *J. Electrochem. Soc.* **1997**, *144(2)*, 485. (b) Lo, Y. L.; Hwang, B. J. *Langmuir* **1998**, *14*, 944.

(25) Messaoudi, B.; Joiret, S.; Keddam, M.; Takenouti, H. *Electrochim. Acta* **2001**, *46*, 2487.

(26) Zahn, D. R. T. *Phys. Status Solidi A* **1995**, *152*, 179.

(27) (a) Cuesta, A.; Gutiérrez, C. *J. Electroanal. Chem.* **1995**, *382*, 153. (b) Caram, J. A.; Gutiérrez, C. *J. Electroanal. Chem.* **1990**, *291*, 289.

(28) (a) Blondeau, G.; Frolicher, M.; Jovancicevic, V.; Hugot-Le Goff, A. *Surf. Sci.* **1979**, *80*, 151. (b) Blackwood, D. J.; Peter, L. M. *Electrochim. Acta* **1990**, *35*, 1073.

Electrochemically Grown Tin Oxide Thin Films

J. Phys. Chem. B, Vol. 108, No. 24, 2004 **8181**

(29) Larramona, G.; Gutiérrez, C. *J. Electrochem. Soc.* **1989**, *136(8)*, 2171.

(30) Larramona, G.; Gutiérrez, C. *J. Electrochem. Soc.* **1990**, *137*, 428.

(31) Aspnes, D. E. *Surf. Sci.* **1973**, *37*, 418.

(32) Kolb, D. M. In *Spectroelectrochemistry: Theory and Practice*; Gale, R. J., Ed.; Plenum: New York, 1988; p 87.

(33) Hirokawa, T.; Yomogita, T.; Honda, K. *Jpn. J. Appl. Phys.* **1970**, *9(10)*, 1210.

(34) Díaz R.; Díez-Pérez, I.; Güell, A. G.; Sanz, F., to be submitted.

(35) Güell, A. G.; Díez-Pérez, I.; Gorostiza, P.; Sanz, F. *Anal. Chem.* in press.

(36) Maya, L. *Inorg. Chem.* **1976**, *15*, 2179.

(37) Yu, K. N.; Xiong, Y.; Liu, Y.; Xiong, C. *Phys. Rev. B* **1997**, *55*, 2666.

(38) Sistiaga, M.; Cuesta, A.; Pierna, A. R.; Gutiérrez, C. *Surf. Sci.* **1998**, *410*, 312.

(39) Boeck, W.; Kolb, D. M. *Surf. Sci.* **1982**, *118*, 613.

(40) Howie, R. A.; Moser, W. *Nature* **1968**, *219*, 372.

(41) *Comprehensive Inorganic Chemistry*; Bailar, J. C., Eméleus, H. J., Nyholm, R., Trotman-Dickenson, A. F., Eds.; Pergamon Press: Oxford, 1973.

(42) Díaz, R. Ph.D. Dissertation, University of Barcelona, 2002.

(43) *Technology of III–V, II–VI and Non-Tetrahedrally Bonded Compounds*; Schulz M., Weiss H., Eds.; Landolt-Börnstein New Series; Springer-Verlag: Berlin, 1984; Vol. 17, subvol. d, p 255.

(44) *Physics of Non-Tetrahedrally Bonded Binary Compounds II*; Madelung, O., Ed.; Landolt-Börnstein New Series; Springer-Verlag: Berlin, 1983; Vol. 17, subvol. F, p 200.

(45) Morrison, S. R. In *Electrochemistry at Semiconductor and Oxidised Metal Electrodes*; Plenum Press: New York, 1980.

(46) Büchler, M.; Schmuki, P.; Böhni, H.; Stenberg, T.; Mäntylä, T. *J. Electrochem. Soc.* **1998**, *145*, 378.

(47) Zuo, J.; Xu, C.; Liu, X.; Wang, C.; Wang, C.; Hu, Y.; Qian, Y. *J. Appl. Phys.* **1994**, *75*, 1835.

(48) Summit, R.; Borrelli, N. F. *J. Appl. Phys.* **1966**, *37*, 2200.